Supporting Information For

Spectroscopic Signature of the Aggregation-Induced Emission Phenomena Caused by Restricted Non-Radiative Decay: A Theoretical Proposal

Tian Zhang,[†,⊥] Huili Ma,[†,⊥] Yingli Niu,[‡] Wenqiang Li,[†] Dong Wang,[†] Qian Peng,*[,‡] Zhigang Shuai,*[,†] and WanZhen Liang[§]

[†]Key Laboratory of Organic OptoElectronics and Molecular Engineering, Department of Chemistry, Tsinghua University, Beijing 100084, P. R. China.

[‡]Key Laboratory of Organic Solids, Beijing National Laboratory for Molecular Science (BNLMS), Institute of Chemistry, Chinese Academy of Sciences, Beijing 100190, P. R. China.

[§]Department of Chemistry, Xiamen University, Xiamen 361005, P. R. China.

[⊥]These authors contributed equally.

I.Complete list of authors for Refs. 4, 13, 28, 32, 36, and 45

4. Chen, S. J.; Hong, Y. N.; Liu, Y.; Liu, J. Z.; Leung, C. W. T.; Li, M.; Kwok, R. T. K.; Zhao, E. G.; Lam, J. W. Y.; Yu, Y.; Tang, B. Z. Full-Range Intracellular pH Sensing by an Aggregation-Induced Emission-Active Two-Channel Ratiometric Fluorogen. *J. Am. Chem. Soc.* **2013**, *135*, 4926-4929.

13. Hu, R. R.; Lager, E.; Aguilar-Aguilar, A.; Liu, J. Z.; Lam, J. W. Y.; Sung, H. H. Y.; Williams, I. D.; Zhong, Y. C.; Wong, K. S.; Peña-Cabrera, E.; Tang, B. Z. Twisted Intramolecular Charge Transfer and Aggregation-Induced Emission of BODIPY Derivatives. *J. Phys. Chem. C* **2009**, *113*, 15845-15853.

28. Dong, Y. Q.; Lam, J. W. Y.; Qin, A. J.; Sun, J. X.; Liu, J. Z.; Li, Z.; Sun, J. Z.; Sung, H. H. Y.; Williams, I. D.; Kwok, H. S.; Tang, B. Z. Aggregation-Induced and Crystallization-Enhanced Emissions of 1,2-Diphenyl-3,4-bis(Diphenylmethylene) -1-Cyclobutene. *Chem. Commun.* **2007**, 3255-3257.

32. Frisch, M. J.; Trucks, G. W.; Schlegel, H. B.; Scuseria, G. E.; Robb, M. A.; Cheeseman, J. R.; Scalmani, G.; Barone, V.; Mennucci, B.; Petersson, G. A.; Nakatsuji, H.; Caricato, M.; Li, X.; Hratchian, H. P.; Izmaylov, A. F.; Bloino, J.; Zheng, G.; Sonnenberg, J. L.; Hada, M.; Ehara, M.; Toyota, K.; Fukuda, R.; Hasegawa, J.; Ishida, M.; Nakajima, T.; Honda, Y.; Kitao, O.; Nakai, H.; Vreven, T.; Montgomery, J. A., Jr.; Peralta, J. E.; Ogliaro, F.; Bearpark, M.; Heyd, J. J.; Brothers, E.; Kudin, K. N.; Staroverov, V. N.; Kobayashi, R.; Normand, J.; Raghavachari, K.; Rendell, A.; Burant, J. C.; Iyengar, S. S.; Tomasi, J.; Cossi, M.; Rega, N.; Millam, M. J.; Klene, M.; Knox, J. E.; Cross, J. B.; Bakken, V.; Adamo, C.; Jaramillo, J.; Gomperts, R.; Stratmann, R. E.; Yazyev, O.; Austin, A. J.; Cammi, R.; Pomelli, C.; Ochterski, J. W.; Martin, R. L.; Morokuma, K.; Zakrzewski, V. G.; Voth, G. A.; Salvador, P.; Dannenberg, J. J.; Dapprich, S.; Daniels, A. D.; Farkas, Ö.; Foresman, J. B.; Ortiz, J. V.; Cioslowski, J.; Fox, D. J. Gaussian 09, Revision D.01, Gaussian, Inc., Wallingford CT, 2009.

36. Sherwood, P.; de Vries, A. H.; Guest, M. F.; Schreckenbach, G.; Catlow, C. R. A.; French, S. A.; Sokol, A. A.; Bromley, S. T.; Thiel, W.; Turner, A. J.; Billeter, S.; Terstegen, F.; Thiel, S.; Kendrick, J.; Rogers, S. C.; Casci, J.; Watson, M.; King, F.; Karlsen, E.; Sjovoll, M.; Fahmi, A.; Schafer, A.; Lennartz C. QUASI: A General Purpose Implementation of the QM/MM Approach and Its Application to Problems in Catalysis. J. Mol. Struct. : Theochem 2003, 632, 1-28.

45. Valiev, M.; Bylaska, E. J.; Govind, N.; Kowalski, K.; Straatsma, T. P.; Van Dam, H. J. J.; Wang, D.; Nieplocha, J.; Apra, E.; Windus, T. L.; de Jong, W. A. NWChem: A Comprehensive and Scalable Open-Source Solution for Large Scale Molecular Simulations. *Comput. Phys. Commun.* **2010**, *181*, 1477-1489.

II. Theoretical Formalism

Radiative and Non-radiative Decay Rates

The radiative decay rate (k_r) with the dimension of s^{-1} can be evaluated through the Einstein

spontaneous emission relationship:[S1,S2]

$$k_{\mathrm{r}} = \frac{fE_{\mathrm{vert}}^{2}}{1.499\ \mathrm{s}\cdot\mathrm{cm}^{-2}} \tag{S1}$$

where f is the dimensionless oscillator strength of the excited (e) state, E_{vert} is the vertical excitation energy from the e state to the ground (g) state with the dimension of cm^{-1}.

Based on Fermi Golden Rule, we apply thermal vibration correlation function formalism to obtain the non-radiative internal conversion rate (k_{ic}):[23,44]

$$k_{\mathrm{ic}} = \sum_{kl} \frac{1}{\hbar^{2}} R_{kl} \int_{-\infty}^{\infty} \mathrm{d}t \left[\mathrm{e}^{i\omega_{\mathrm{if}} t} Z_{\mathrm{i}}^{-1} \rho_{\mathrm{ic},kl}\left(t,T\right) \right] \tag{S2}$$

More details of the correlation function part $\rho_{\mathrm{ic},kl}\left(t,T\right)$ are given in our previous work.[33] The normal-mode coordinates of g state and e state are correlated through the Duschinsky rotation matrix $\bar{S}$ with the relationship $Q_{\mathrm{e}} = \bar{S}Q_{\mathrm{g}} + \bar{\Delta}$. The vector $\bar{\Delta}$ is the displacement along the normal mode j between the minima of the g and e. Δ is the dimensionless displacement with the definition of $\Delta_{j} = \sqrt{\omega_{\mathrm{e}}^{j}}\bar{\Delta}_{j}$. $\bar{S}$ and $\bar{\Delta}$ are calculated through DUSHIN program.[60,61]

We applied the first-order perturbation theory to compute the nonadiabatic coupling matrix elements (NACMEs) following Lin.[58] Express it at the equilibrium position approximately,

$$\left\langle \Phi_{\mathrm{f}} \middle| \hat{P}_{\mathrm{f}l} \middle| \Phi_{\mathrm{i}} \right\rangle = -i\hbar \left\langle \Phi_{\mathrm{f}} \middle| \frac{\partial}{\partial Q_{\mathrm{f}l}} \middle| \Phi_{\mathrm{i}} \right\rangle = -i\hbar \frac{\left\langle \Phi_{\mathrm{f}}^{0} \middle| \partial\hat{U} / \partial Q_{\mathrm{f}l} \middle| \Phi_{\mathrm{i}}^{0} \right\rangle}{E_{\mathrm{i}}^{0} - E_{\mathrm{f}}^{0}} \tag{S3}$$

where

$$\left\langle \Phi_{\mathrm{f}}^{0} \middle| \partial\hat{U} / \partial Q_{\mathrm{f}l} \middle| \Phi_{\mathrm{i}}^{0} \right\rangle = -\sum_{\sigma} \frac{Z_{\sigma}\mathrm{e}^{2}}{\sqrt{M_{\sigma}}} \sum_{\tau=x,y,z} E_{\mathrm{f}\leftarrow\mathrm{i},\sigma\tau} L_{\sigma\tau,l} \tag{S4}$$

The transition electric field $E_{\mathrm{f}\leftarrow\mathrm{i},\sigma\tau} = \int \mathrm{d}\boldsymbol{r}\rho_{\mathrm{fi}}^{0}(\boldsymbol{r}) \frac{\mathrm{e}(r_{\tau} - R_{\sigma\tau})}{\left|\boldsymbol{r} - \boldsymbol{R}_{\sigma}\right|^{3}}$ can be computed directly from TD-PBE0 calculation using D.01 version of Gaussian 09 package, and U is the electron-nuclear potential term in

the Hamiltonian. Recently Send and Furche also produced exact analytical derivative couplings [S3] in a finite atom-centered basis set, which has been implemented in Turbomole. We used the former scheme to deal with the solution phase as well as the solid phases. We care the comparison, therefore either scheme is effective.

Resonance Raman Spectroscopy (RRS)

RRS was obtained by using the analytical expression in the time domain.[S4,62] The RRS cross section $\sigma(\omega_{\mathrm{I}},\omega_{\mathrm{S}})$ is given as follows:

$$\sigma(\omega_{\mathrm{I}},\omega_{\mathrm{S}}) \propto \omega_{\mathrm{I}}\omega_{S}^{3} S(\omega_{\mathrm{I}},\omega_{\mathrm{S}}) \tag{S5}$$

where ω_{I} is the frequency of the incident light, ω_{S} is the frequency of the scattered light. The line shape $S(\omega_{\mathrm{I}},\omega_{\mathrm{S}})$ can be written as

$$S(\omega_{\mathrm{I}},\omega_{\mathrm{S}}) = 2\pi\sum_{m,n} P(n)\left|\hat{e}_{\mathrm{S}}\cdot\alpha_{mn}\cdot\hat{e}_{\mathrm{I}}\right|^{2}\delta(\omega_{\mathrm{S}}-\omega_{\mathrm{I}}-\varepsilon_{n}+\varepsilon_{m}) \tag{S6}$$

$\hat{e}_{\mathrm{I}}$ and $\hat{e}_{\mathrm{S}}$ indicate the polarization directions of the incident light and the scattered light. The single molecule vibrate could be detected by the change of the vibrational state on the electronic g state from the initial n to the final m. ε_{n} and ε_{m} are the corresponding vibrational energies. α_{mn} is the Kramers-Heisenberg-Dirac (KHD) polarizability tensor.

Considering the "resonant" conditions and a single resonant electronic state $|\mathrm{e}\rangle$ with the vibrational state k_{e}, we get

$$\alpha_{mn} = \sum_{k_{\mathrm{e}}} \frac{\langle m|\mu_{\mathrm{eg}}|k_{\mathrm{e}}\rangle\langle k_{\mathrm{e}}|\mu_{\mathrm{eg}}|n\rangle}{\omega_{nk_{\mathrm{e}}}-\omega_{\mathrm{I}}-i\gamma} \tag{S7}$$

μ_{eg} is the electric transition dipole moment between the two electronic states $|\mathrm{g}\rangle$ and $|\mathrm{e}\rangle$, and $\omega_{nk_{\mathrm{e}}} = \omega_{\mathrm{eg}} + \varepsilon_{k_{\mathrm{e}}} - \varepsilon_{n}$. ω_{eg} is the electronic adiabatic energy difference. γ is the damping constant of

the excited state. For strong-dipole allowed transition, only the Frank-Condon (FC) term is considered approximately, eq S7 becomes

$$\alpha_{mn}^{\mathrm{FC}} = \mu_0^2 \sum_{k_\mathrm{e}} \frac{\langle m | k_\mathrm{e} \rangle \langle k_\mathrm{e} | n \rangle}{\omega_{nk_\mathrm{e}} - \omega_\mathrm{I} - i\gamma} \tag{S8}$$

By transforming $\alpha_{mn}^{\mathrm{FC}}$ into the time domain using the Green's function, we obtain

$$\alpha_{mn}^{\mathrm{FC}} = i|\boldsymbol{\mu}_0|^2 \int_0^\infty G_{mn}(t) \exp\left[i\left(\omega_\mathrm{I} - \omega_\mathrm{eg} + \varepsilon_n\right)t - \gamma t \right] \mathrm{d}t \tag{S9}$$

$G_{mn}(t)$ has an analytical solution for the *j*th single-mode excitation from *n* to *m*,

$$\begin{aligned} G_{mn}(t) &= \sigma_0(t) W_{mn}(t) \\ \sigma_0(t) &= |\Psi(t)|^{-1/2} \exp\left[\Delta^T f(t) \Delta\right] \\ W_{mn}(t) &= \left(m!n!2^{m+n}\right)^{-1/2} \left[\beta(t)\right]^{m+n} \sum_{k=0}^{k^*} \frac{(2k)!}{k!} \eta_{mnk} \left[\zeta(t)\right]^k \times H_{m+n-2k}\left[\frac{S^T f(t) \Delta}{\beta(t)}\right] \end{aligned} \tag{S10}$$

S is defined as $S_{ij} = \sqrt{\omega_\mathrm{e}^i / \omega_\mathrm{g}^j}\, \bar{S}_{ij}$. Δ and $\bar{S}$ are the dimensionless displacement and the Duschinsky rotation matrix following the algorithm used in the rate constant calculation. $H_p[z]$ is the Hermite polynomial, k^* is the integer part of $\frac{m+n}{2}$.

$$\begin{aligned} \eta_{mnk} &= \sum_{q=0}^{2k} (-1)^q C_m^{2k-q} C_q^n = \sum_{q=0}^{2k} (-1)^q \frac{m!}{(2k-q)!(m-2k+q)!} \times \frac{q!}{n!(q-n)!} \\ \Psi(t) &= \frac{1}{4} U^{-1} V^{-1} \\ f(t) &= -(S^{-1})^T U C_- \\ \beta(t) &= \left[\frac{1}{2} - \left(U C_+ (S^{-1})^T\right)_{jj}\right]^{1/2} \\ \zeta(t) &= -\frac{1 - 2\left(V C_- (S^{-1})^T\right)_{jj}}{1 - 2\left(U C_+ (S^{-1})^T\right)_{jj}} \end{aligned} \tag{S11}$$

with

$$\begin{aligned} C_\pm &= 1 \pm e^{-i\omega_\mathrm{e} t} \\ U &= \left(C_+ (S^{-1})^T + C_- S\right)^{-1} \\ V &= \left(C_+ S + C_- (S^{-1})^T\right)^{-1} \end{aligned} \tag{S12}$$

Relationship between the RRS Intensity σ and the Relaxation Energy of Each Mode λ_j

Excluding mode distortion and Duschinsky rotation ($\omega_{\mathrm{g}}^{j}=\omega_{\mathrm{e}}^{j},\bar{S}=\mathrm{I}$), we get $C_{\pm}=1\pm e^{-i\omega_{\mathrm{g}}^{j}t},U=\frac{1}{2},V=\frac{1}{2},\Psi(t)=1,f(t)=-\frac{1}{2}\left(1-e^{-i\omega_{\mathrm{g}}^{j}t}\right),\beta(t)=\left[-\frac{1}{2}e^{-i\omega_{\mathrm{g}}^{j}t}\right]^{1/2},\zeta(t)=1$. Only fundamental $0\rightarrow 1$ transitions are considered, $m=1,n=0$,

$$\begin{aligned}&k^{*}=0\\&\eta_{100}=1\end{aligned}\tag{S13}$$

$$\begin{aligned}G_{10}(t)&=\exp\left[\Delta^{T}f(t)\Delta\right]2^{-1/2}\beta(t)\times H_{1}\left[\frac{f(t)\Delta}{\beta(t)}\right]\\&=\exp\left[\Delta^{T}f(t)\Delta\right]2^{-1/2}\beta(t)\times 2\frac{f(t)\Delta}{\beta(t)}\\&=\sqrt{2}\exp\left[\Delta_{j}^{2}f(t)\right]f(t)\Delta_{j}\\&=-\frac{\sqrt{2}\Delta_{j}}{2}\left(1-e^{-i\omega_{\mathrm{g}}^{j}t}\right)\exp\left[-\frac{\Delta_{j}^{2}}{2}\left(1-e^{-i\omega_{\mathrm{g}}^{j}t}\right)\right]\end{aligned}\tag{S14}$$

The short time approximation ($e^{-i\omega_{\mathrm{g}}^{j}t}\approx 1-i\omega_{\mathrm{g}}^{j}t$) is adopted,

$$G_{10}(t)=-\frac{\sqrt{2}\Delta_{j}}{2}i\omega_{\mathrm{g}}^{j}t\times\exp\left[-\frac{\Delta_{j}^{2}}{2}i\omega_{\mathrm{g}}^{j}t\right]\tag{S15}$$

Then, the KHD polarizability tensor can be written as,

$$\begin{aligned}\alpha_{10}^{\mathrm{FC}}&=i\left|\boldsymbol{\mu}_{0}\right|^{2}\int_{0}^{\infty}G_{10}(t)\exp\left[i\left(\omega_{\mathrm{I}}-\omega_{\mathrm{eg}}+\varepsilon_{0}\right)t-\gamma t\right]\mathrm{d}t\\&=i\left|\boldsymbol{\mu}_{0}\right|^{2}\int_{0}^{\infty}-\frac{\sqrt{2}\Delta_{j}}{2}i\omega_{\mathrm{g}}^{j}t\times\exp\left[-\frac{\Delta_{j}^{2}}{2}i\omega_{\mathrm{g}}^{j}t\right]\exp\left[i\left(\omega_{\mathrm{I}}-\omega_{\mathrm{eg}}+\frac{1}{2}\omega_{\mathrm{g}}^{j}\right)t-\gamma t\right]\mathrm{d}t\\&=-\frac{i\left|\boldsymbol{\mu}_{0}\right|^{2}\Delta_{j}\omega_{\mathrm{g}}^{j}}{\sqrt{2}}\int_{0}^{\infty}it\times\exp\left[i\left(\omega_{\mathrm{I}}-\omega_{\mathrm{eg}}+\frac{1}{2}\omega_{\mathrm{g}}^{j}-\frac{\Delta_{j}^{2}}{2}\omega_{\mathrm{g}}^{j}\right)t-\gamma t\right]\mathrm{d}t\end{aligned}\tag{S16}$$

Under pre-resonance conditions $\omega_{\mathrm{eg}}-\omega_{\mathrm{I}}>>\omega_{\mathrm{g}}^{j}$ and $\Delta_{j}<<1$, we also ignore the influence of the damping factor γ in this situation,

$$
\begin{aligned}
\alpha_{10}^{FC} &= -\frac{i\left|\boldsymbol{\mu}_0\right|^2 \Delta_j \omega_{\mathrm{g}}^j}{\sqrt{2}} \int_0^{\infty} it \times \exp\left[i\left(\omega_{\mathrm{I}} - \omega_{\mathrm{eg}} + \frac{1}{2}\omega_{\mathrm{g}}^j - \frac{\Delta_j^2}{2}\omega_{\mathrm{g}}^j \right) t - \gamma t \right] \mathrm{d}t \\
&= -\frac{\left|\boldsymbol{\mu}_0\right|^2 \Delta_j \omega_{\mathrm{g}}^j}{\sqrt{2}} \int_0^{\infty} it \times \mathrm{e}^{-(\omega_{\mathrm{eg}}-\omega_{\mathrm{I}})it} \mathrm{d}(\mathrm{i}t) \\
&= -\frac{\left|\boldsymbol{\mu}_0\right|^2 \Delta_j \omega_{\mathrm{g}}^j}{\sqrt{2}(\omega_{\mathrm{eg}}-\omega_{\mathrm{I}})^2} \int_0^{\infty} (\omega_{\mathrm{eg}}-\omega_{\mathrm{I}}) it \times \mathrm{e}^{-(\omega_{\mathrm{eg}}-\omega_{\mathrm{I}})it} \mathrm{d}[(\omega_{\mathrm{eg}}-\omega_{\mathrm{I}})(\mathrm{i}t)] \\
&= -\frac{\left|\boldsymbol{\mu}_0\right|^2 \Delta_j \omega_{\mathrm{g}}^j}{\sqrt{2}(\omega_{\mathrm{eg}}-\omega_{\mathrm{I}})^2} \times 1 \\
&= -\frac{\left|\boldsymbol{\mu}_0\right|^2}{\sqrt{2}(\omega_{\mathrm{eg}}-\omega_{\mathrm{I}})^2} \times \Delta_j \omega_{\mathrm{g}}^j
\end{aligned}
\tag{S17}
$$

Then, the relationship between the intensity of the RRS and the relaxation energy of each mode can be obtained considering the above approximations.

$$
\begin{aligned}
&\sigma \propto \omega_{\mathrm{I}} \omega_{\mathrm{S}}^3 \left|\alpha_{10}^{FC}\right|^2 = \frac{\omega_{\mathrm{I}} \omega_{\mathrm{S}}^3 \left|\boldsymbol{\mu}_0\right|^4}{2(\omega_{\mathrm{eg}}-\omega_{\mathrm{I}})^4} \times \Delta_j^2 \omega_{\mathrm{g}}^{j2} = \frac{\omega_{\mathrm{I}} \omega_{\mathrm{S}}^3 \left|\boldsymbol{\mu}_0\right|^4}{(\omega_{\mathrm{eg}}-\omega_{\mathrm{I}})^4} \times \lambda_g^j \omega_{\mathrm{g}}^j \\
&\Rightarrow \sigma \propto \lambda_g^j \omega_{\mathrm{g}}^j \Rightarrow \frac{\sigma}{\omega_{\mathrm{g}}^j} \propto \lambda_g^j
\end{aligned}
\tag{S18}
$$

Immediately, a direct relationship between the RRS intensity $\sigma(\omega_j)$ and the relaxation energy of each mode (λ_j) is established.

III. Rationalization of the AIE Mechanism from Structure Insight

The relaxation energy reflects the geometric modification during the excited-state decay process. We present the structural parameters **S_0**(**S_1**), the structural difference |Δ(**S_0**-**S_1**)|, and the X-ray crystal structure (Crystal) of **HPDMCb** and **DCPP** at their optimized **S_0**(**S_1**) geometries in Table S7-S8. The optimized structure at the minimum of **S_0** agree well with the crystal structure, which indicates the reliability of our QM/MM method. We find there is little difference in |Δ(**S_0**-**S_1**)| between the solution-phase and solid-phase bond lengths and bond angles. The major difference comes from the

dihedral angles associated with ring twisting motions. There are insignificant geometric changes (less than 1°) for **DCPP** from $\mathbf{S_0}$ to $\mathbf{S_1}$. We then plot the selected dihedral angles with major geometric changes for **HPDMCb** in Figure S11, almost symmetrical dihedrals are not shown for clarity. By analyzing $|\Delta(\mathbf{S_0}\text{-}\mathbf{S_1})|$ in both solution and solid phases, we find: (i) for **HPDMCb**, the dihedral angles between the cyclobutene core and two phenyl rings at the 1,6-positions show much larger modifications than 2,5-positions and 3,4-positions. It suggests that the phenyl rings at the 1,6-positions of **HPDMCb** are largely hindered in solid phase, and theses positions are expected to play dominant roles in the optical properties. (ii) By comparing the difference in the $\mathbf{S_0}$ structure from the solution phase to the solid state with that in the $\mathbf{S_1}$ structure, we can see: the $\mathbf{S_1}$ structure changes much more than the $\mathbf{S_0}$ structure for both **HPDMCb**, indicating the wavelength (energy) change in emission is larger than in absorption. For example, at the $\mathbf{S_0}$ optimized geometry, the dihedral angle at the 1-position of **HPDMCb** becomes slightly planar from solution to solid, in correspondance to the slight red shift in absorption. While at the $\mathbf{S_1}$ optimized geometry, that dihedral angle becomes much more non-planar, in accordance with the calculated remarkable blue-shifted emission. The above mentioned restricted geometric change and large excited-state non-planar modification in solid phase result in the decreased relaxation energy, tending to reduce the Stokes shift and suppress the non-radiative energy disspation channel. These results confirm the dominator roles of the phenyl rings at the "active" positions, which govern the optical properties in the multi-ring compounds. While the remaining rings at the "quiet" positions play the protector roles, which twist the molecular structure to impede effective π-π stacking to form excimers.

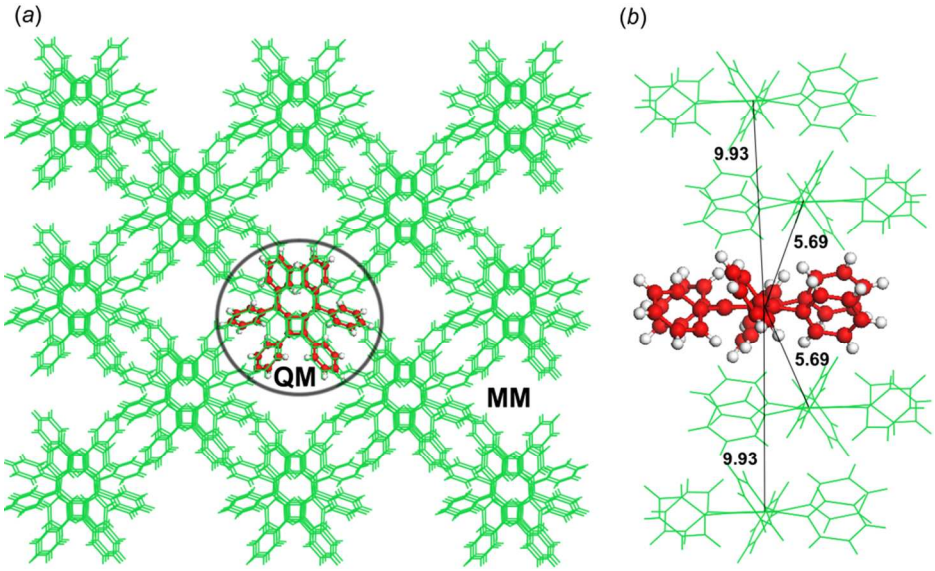

Figure S1 (*a*) Setup of the QM/MM model for **HPDMCb**: a cluster of 65 molecules consisting of 72 QM atoms and 4608 MM atoms. (*b*) Close look at the packing structures and the intermolecular distances (Å) within 10.00 Å of the QM centroid.

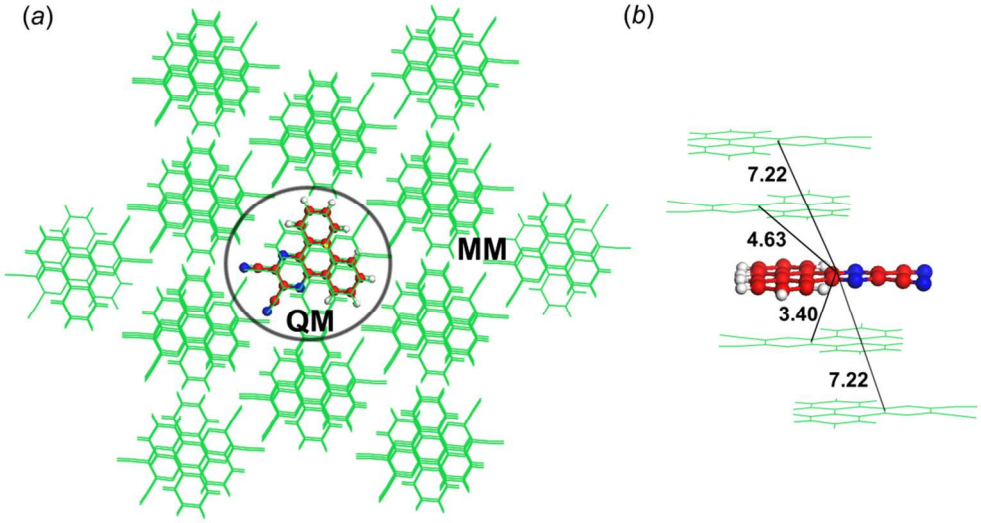

Figure S2 (*a*) Setup of the QM/MM model for **DCPP**: a cluster of 59 molecules consisting of 30 QM atoms and 1740 MM atoms. (*b*) Close look at the packing structures and the intermolecular distances (Å) within 9.00 Å of the QM centroid.

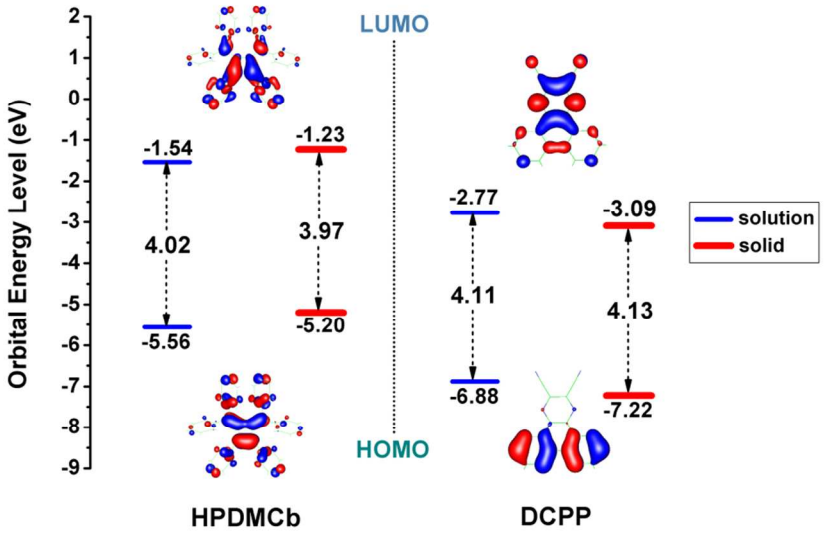

Figure S3 HOMO and LUMO energy levels, HOMO-LUMO energy gaps, HOMO and LUMO contours for **HPDMCb** and **DCPP** at their $\mathbf{S_0}$ equlibrium geometries in both solution and solid phases.

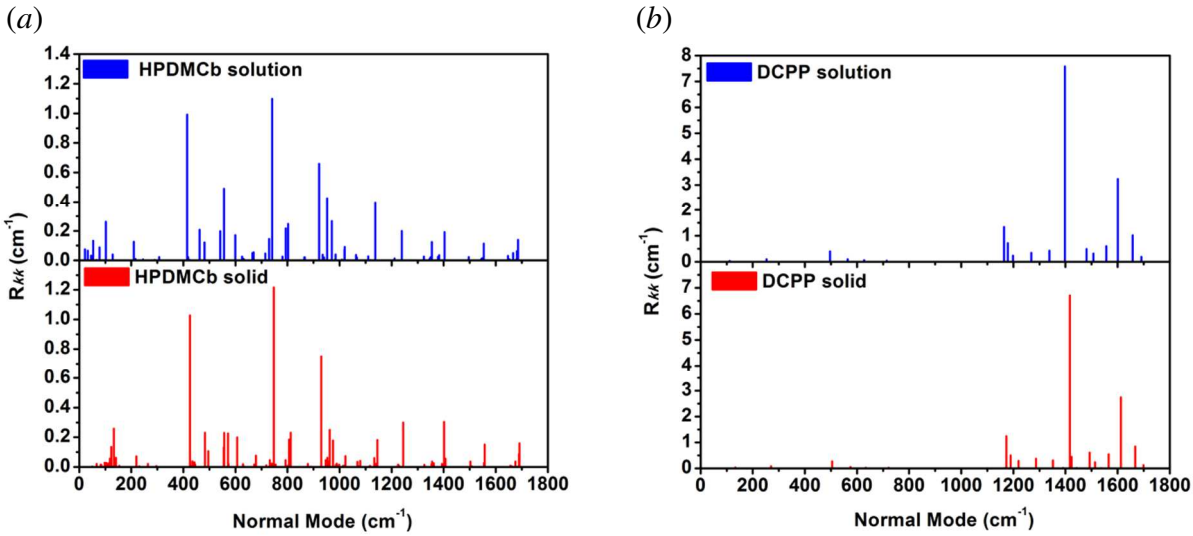

Figure S4 Diagonal elements R_{kk} of the pre-factor (R_{kl}) versus the normal mode frequencies for **HPDMCb** (*a*) and **DCPP** (*b*) in both solution and solid phases.

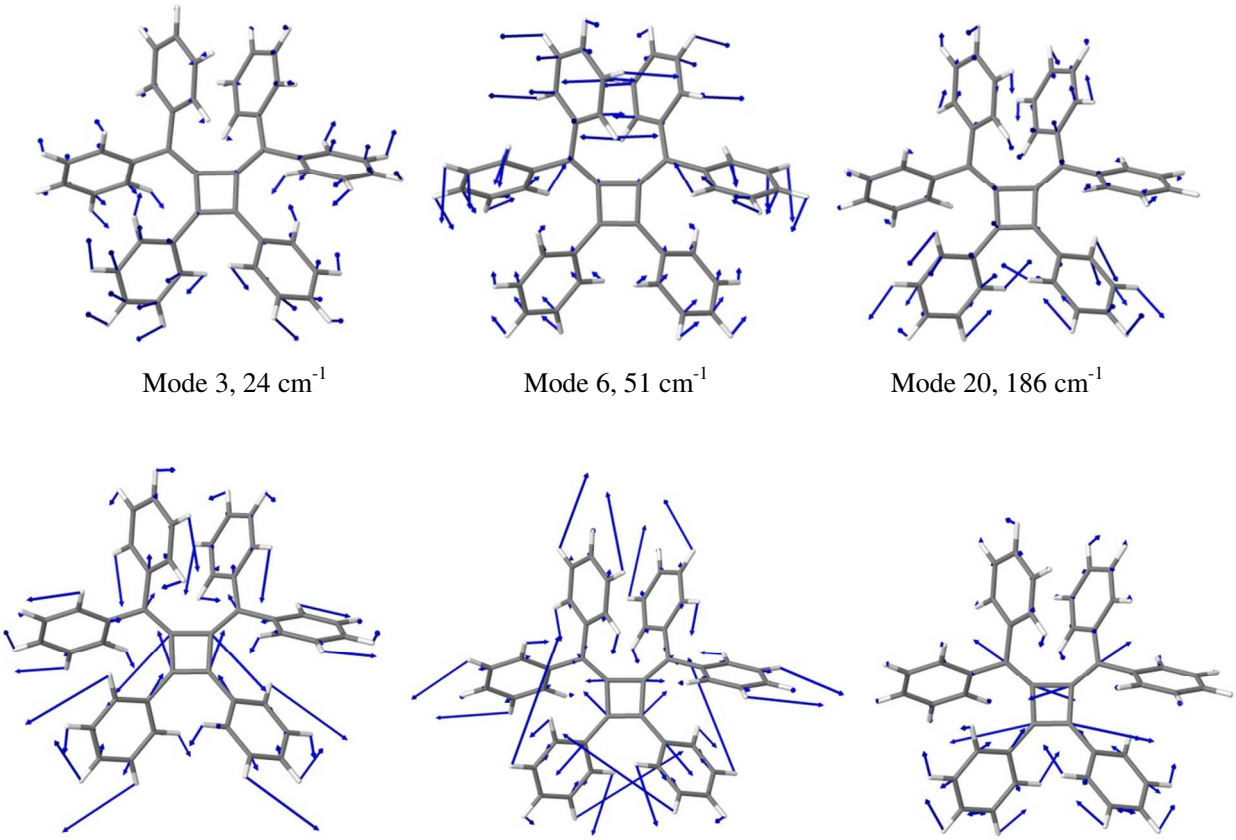

Mode 3, 24 cm^{-1} Mode 6, 51 cm^{-1} Mode 20, 186 cm^{-1}

Mode 116, 1097 cm^{-1} Mode 136, 1215 cm^{-1} Mode 166, 1624 cm^{-1}

Figure S5 Diagrammatic illustration of selected normal modes with large relaxation energies (λ_j) for $\mathbf{S_0}$ of solution-phase **HPDMCb**.

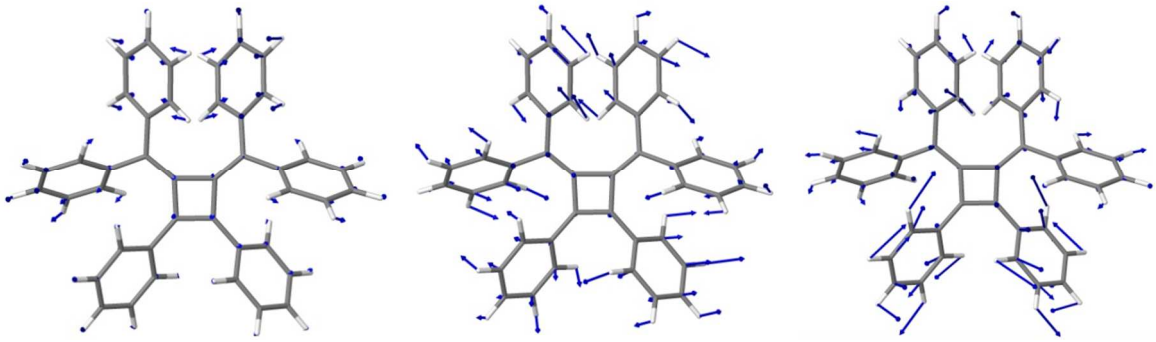

Mode 4, 70 cm^{-1} Mode 16, 141 cm^{-1} Mode 20, 205 cm^{-1}

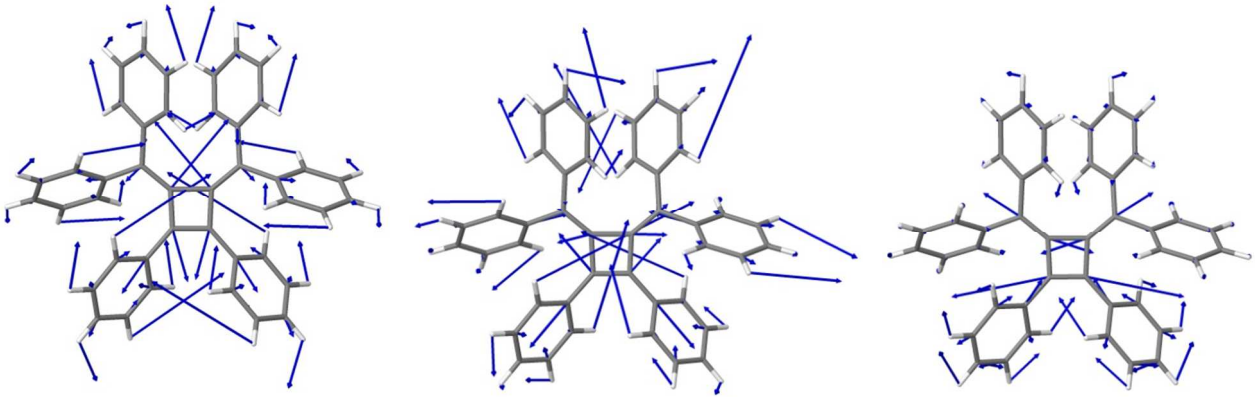

Mode 116, 1101 cm^{-1} Mode 129, 1218 cm^{-1} Mode 166, 1634 cm^{-1}

Figure S6 Diagrammatic illustration of selected normal modes with large relaxation energies (λ_j) for $\mathbf{S_0}$ of solid-phase **HPDMCb**.

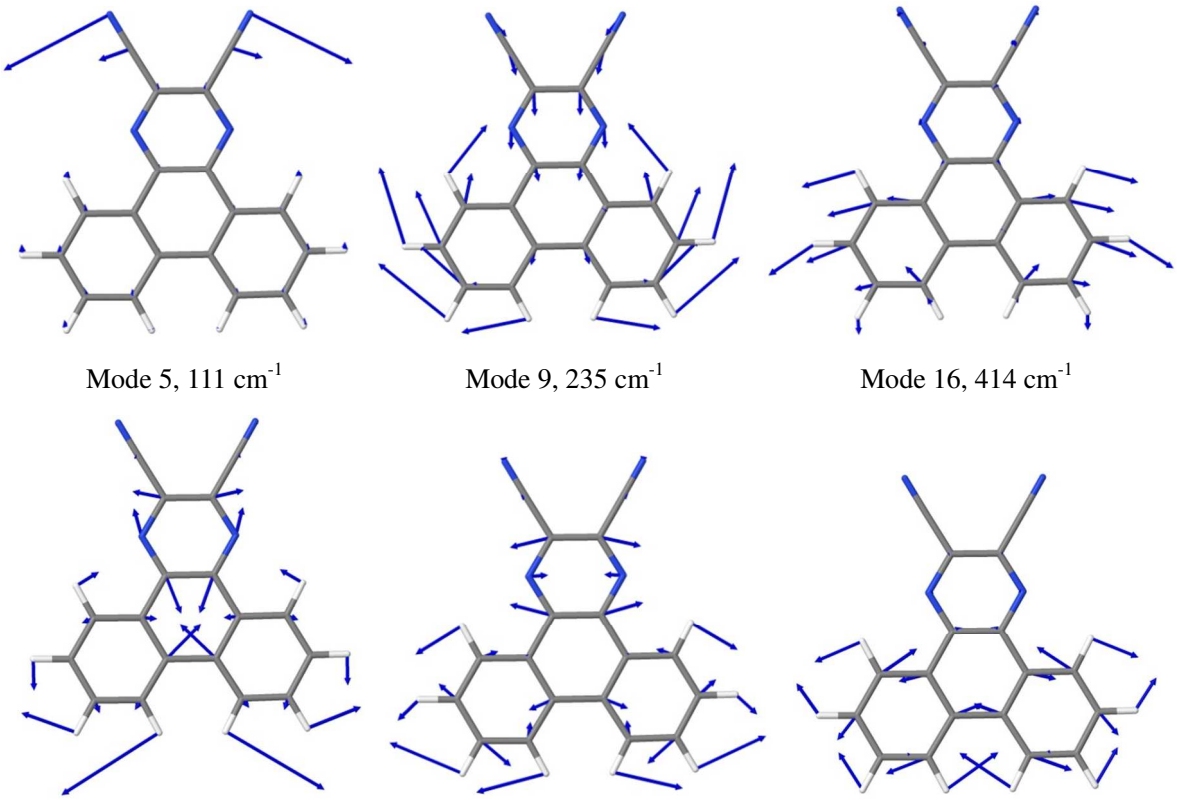

Mode 5, 111 cm^{-1} Mode 9, 235 cm^{-1} Mode 16, 414 cm^{-1}

Mode 57, 1312 cm^{-1} Mode 69, 1589 cm^{-1} Mode 73, 1684 cm^{-1}

Figure S7 Diagrammatic illustration of selected normal modes with large relaxation energies (λ_j) for $\mathbf{S_0}$ of solution-phase **DCPP**.

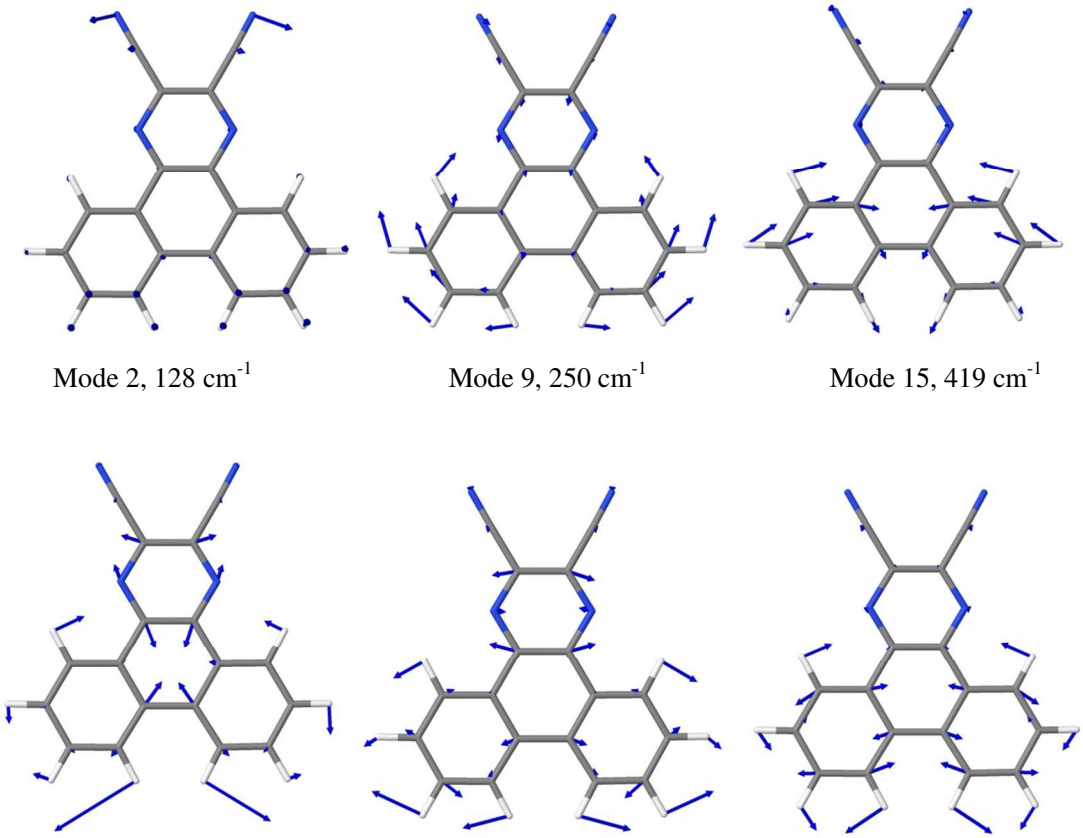

Figure S8 Diagrammatic illustration of selected normal modes with large relaxation energies (λ_j) for $\mathbf{S_0}$ of solid-phase **DCPP**.

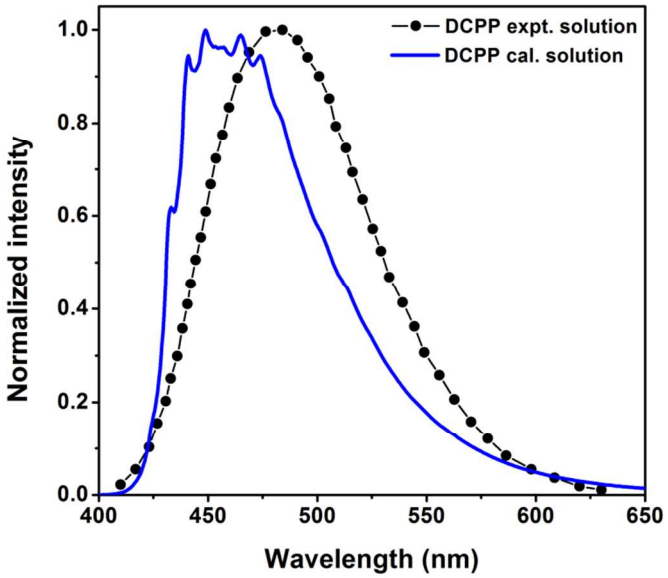

Figure S9 Comparison of optical emission spectrum between experiment (expt.) and calculation (cal.) for **DCPP** in THF solution (T = 300 K). Mode distortion and Duschinsky rotation effects are included.

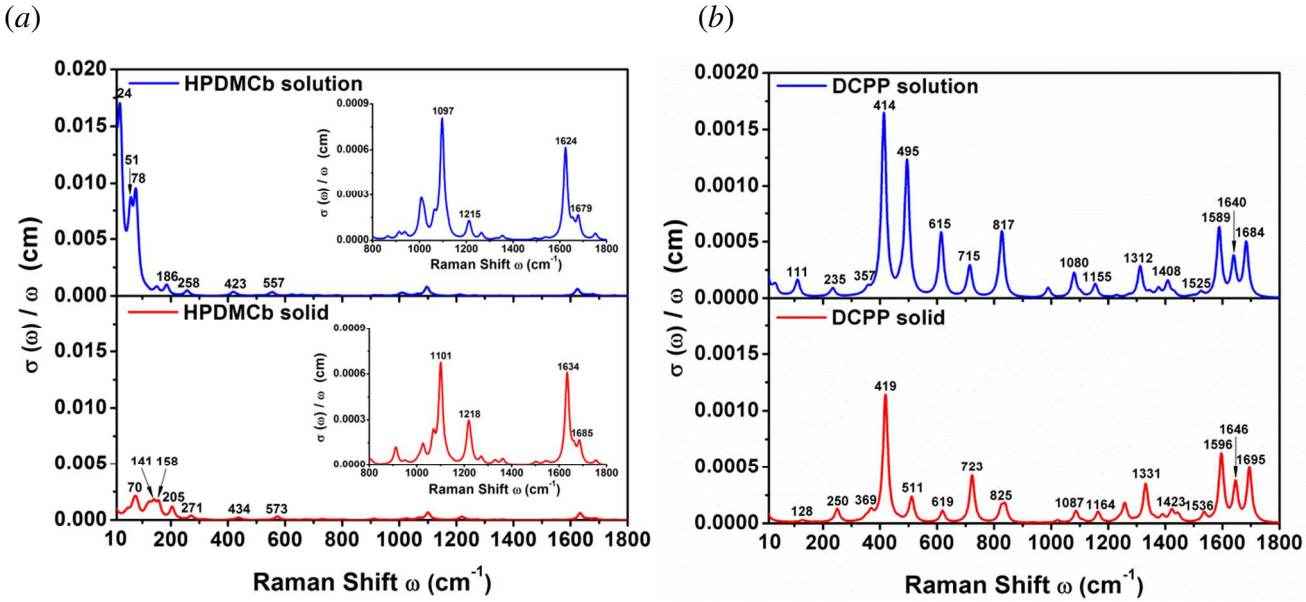

Figure S10 Calculated [$\sigma(\omega)$ / ω] versus ω in both the solution and solid phases for **HPDMCb** (*a*) and **DCPP** (*b*).

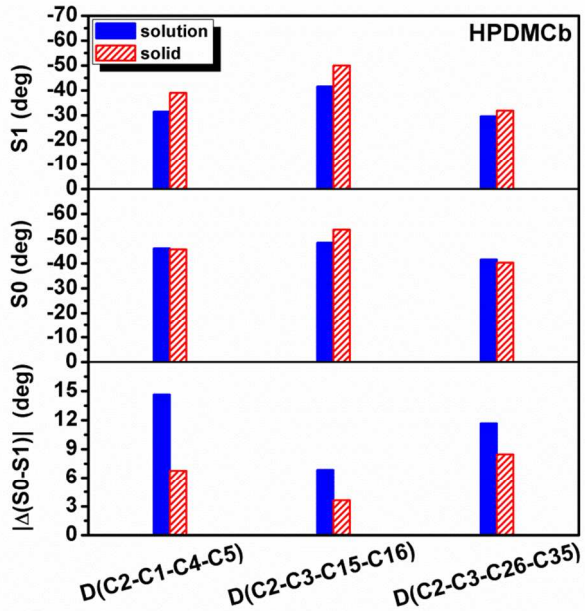

Figure S11 Dihedral angles (degree) at the 1-position (C2-C1-C4-C5), 2-position (C2-C3-C15-C16) and 3-position (C2-C3-C26-C35) at their $\mathbf{S_0}$($\mathbf{S_1}$) optimized geomtries, dihedral angle modifications |Δ($\mathbf{S_0}$-$\mathbf{S_1}$)| (degree) for **HPDMCb** in both solution and solid phases.

(*a*)

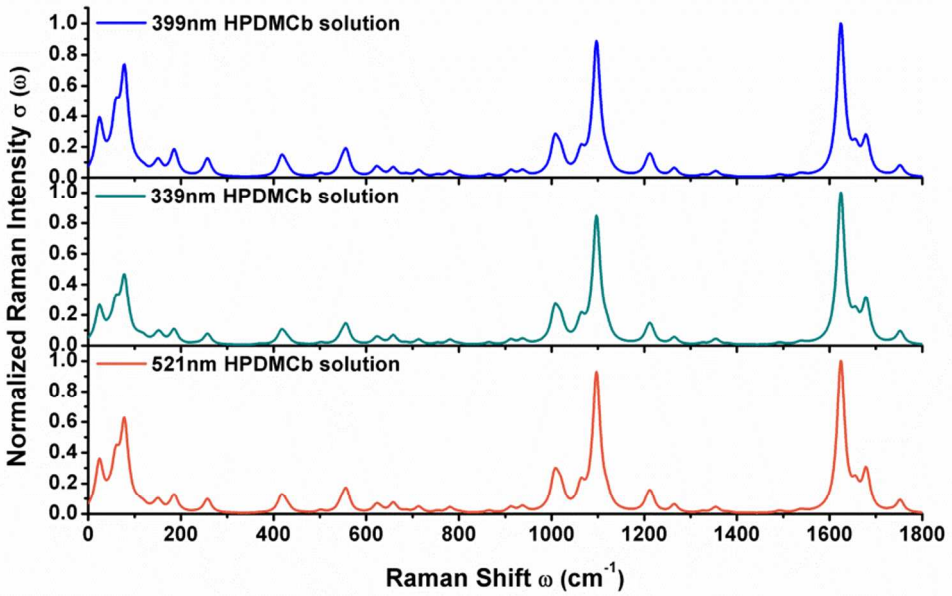

(*b*)

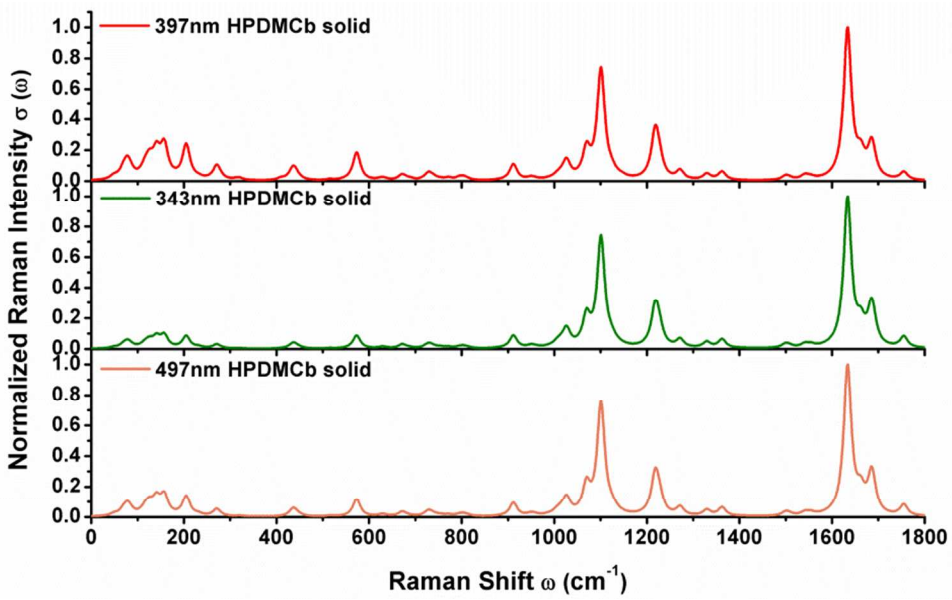

Figure S12 Calculated RRS of **HPDMCb** with the incident wavelength of 399nm, 339nm and 521nm in solution (*a*) and 397nm, 343nm and 497nm in solid (*b*).

(*a*)

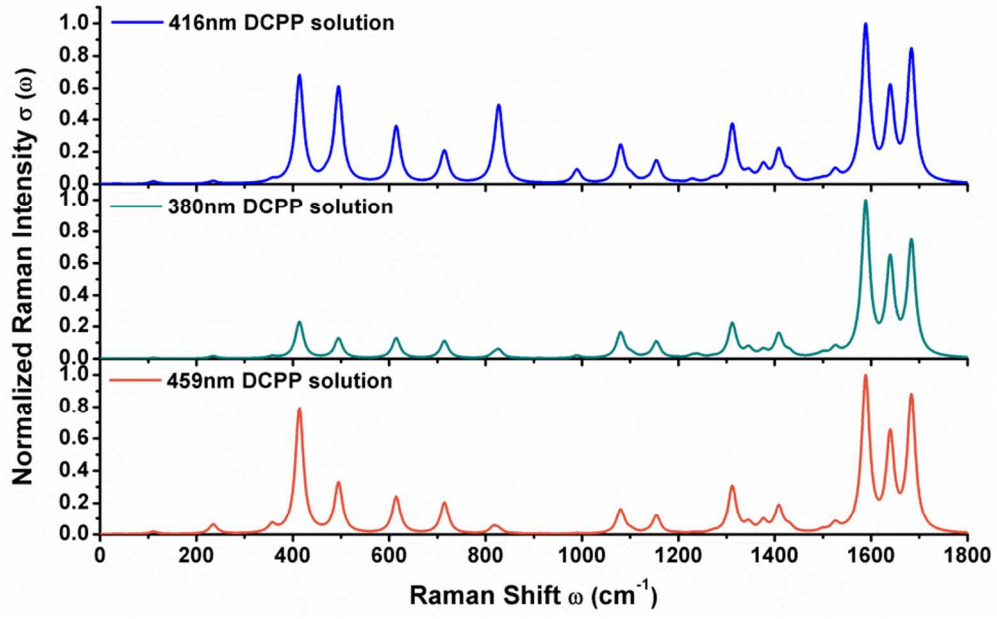

(*b*)

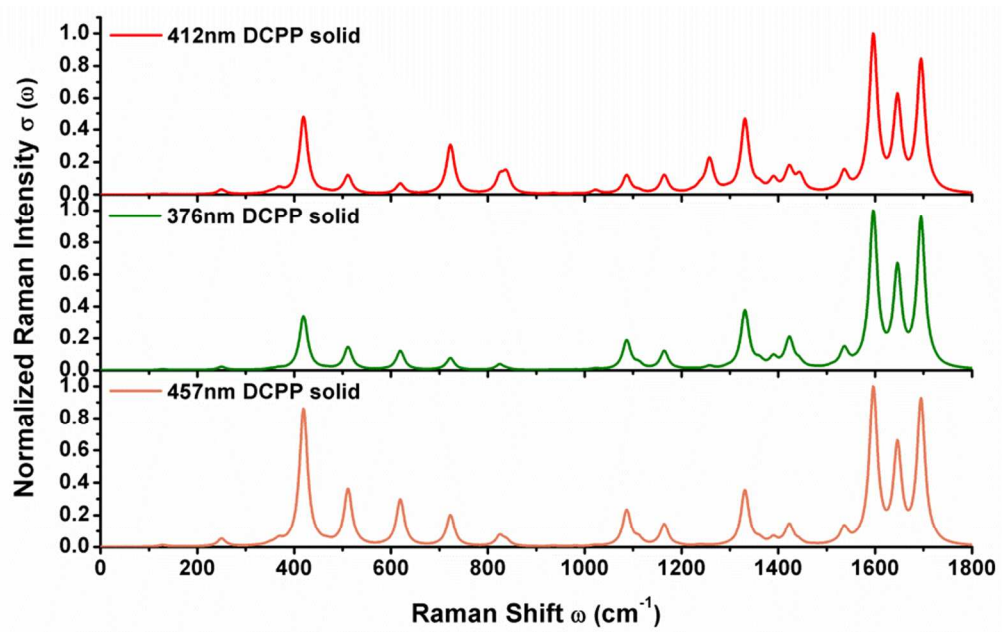

Figure S13 Calculated RRS of **DCPP** with the incident wavelength of 416nm, 380nm and 459nm in solution (*a*) and 412nm, 376nm and 457nm in solid (*b*).

Table S1 $\lambda_{g(e)}$ obtained by normal mode analysis for **HPDMCb** and **DCPP** in both solution and solid phases at the PBE0/6-31G* level.

	HPDMCb		**DCPP**	
	solution	solid	solution	solid
λ_g (meV)	580	530	279	296
λ_e (meV)	680	580	277	293

Table S2 Intermolecular distance (Figure S1-S2) versus the Coulomb coupling component of the excitonic coupling (J_{coul}) in **HPDMCb** and **DCPP** cluster.

HPDMCb		**DCPP**	
Distance (Å)	J_{coul} (meV)	Distance (Å)	J_{coul} (meV)
5.69	27.06	3.40	10.94
9.93	9.18	4.63	3.33
		7.22	3.98

Table S3 The vertical transition energies for solution-phase **HPDMCb** calculated by using methods of PBE0/LR-PCM, PBE0/SS-PCM, CAM-B3LYP/LR-PCM and CAM-B3LYP/SS-PCM based on the PBE0/LR-PCM optimized $\mathbf{S_0}$ and $\mathbf{S_1}$ structures. The experimental values (expt.) are also given.

	absorption			emission		
	PBE0	CAM-B3LYP	expt.	PBE0	CAM-B3LYP	expt.
LR-PCM	3.26 eV	3.62 eV	N. A.	2.09 eV	2.37 eV	N. A.
	(381 nm)	(342 nm)		(592 nm)	(523 nm)	
SS-PCM	3.15 eV	3.66 eV		2.09 eV	2.38 eV	
	(393 nm)	(339 nm)		(594 nm)	(521 nm)	

Table S4 The vertical transition energies for solid-phase **HPDMCb** calculated by using methods of PBE0/QMMM, CAM-B3LYP/QMMM based on the PBE0/QMMM optimized $\mathbf{S_0}$ and $\mathbf{S_1}$ structures. The experimental values (expt.) are also given.

	absorption			emission		
	PBE0	CAM-B3LYP	expt.	PBE0	CAM-B3LYP	expt.
QM/MM	3.24 eV	3.61 eV	3.50 eV	2.27 eV	2.49 eV	2.62 eV
	(383 nm)	(343 nm)	(354 nm)	(547 nm)	(497 nm)	(474 nm)

Table S5 The vertical transition energies for solution-phase **DCPP** calculated by using methods of PBE0/LR-PCM, PBE0/SS-PCM, CAM-B3LYP/LR-PCM and CAM-B3LYP/SS-PCM based on the PBE0/LR-PCM optimized $\mathbf{S_0}$ and $\mathbf{S_1}$ structures. The experimental values (expt.) are also given.

	absorption			emission		
	PBE0	CAM-B3LYP	expt.	PBE0	CAM-B3LYP	expt.
LR-PCM	3.26 eV	3.80 eV	3.20 eV	2.70 eV	3.28 eV	2.57 eV
	(380 nm)	(326 nm)	(388 nm)	(459 nm)	(378 nm)	(482 nm)
SS-PCM	2.87 eV	3.67 eV		1.89 eV	2.38 eV	
	(431 nm)	(338 nm)		(656 nm)	(521 nm)	

Table S6 The vertical transition energies for solid-phase **DCPP** calculated by using methods of PBE0/QMMM, CAM-B3LYP/QMMM based on the PBE0/QMMM optimized $\mathbf{S_0}$ and $\mathbf{S_1}$ structures. The experimental values (expt.) are also given.

	absorption			emission		
	PBE0	CAM-B3LYP	expt.	PBE0	CAM-B3LYP	expt.
QM/MM	3.30 eV	3.88 eV	N. A.	2.71 eV	3.28 eV	2.46 eV
	(376 nm)	(320 nm)		(457 nm)	(378 nm)	(505 nm)

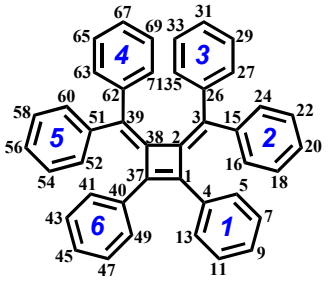

HPDMCb

Table S7 Selected bond lengths (in Å), bond angles (in deg) and dihedral angles (in deg) of solution-phase and solid-phase **HPDMCb** at the $\mathbf{S_0}$ ($\mathbf{S_1}$) optimized geometry.

	solution phase			solid phase			
	$\mathbf{S_0}$	$\mathbf{S_1}$	$\lvert\Delta(\mathbf{S_0}\text{-}\mathbf{S_1})\rvert$	$\mathbf{S_0}$	$\mathbf{S_1}$	$\lvert\Delta(\mathbf{S_0}\text{-}\mathbf{S_1})\rvert$	Crystal[a]
C1-C2	1.48	1.42	0.06	1.49	1.43	0.06	1.50
C37-C38	1.48	1.42	0.06	1.49	1.43	0.06	1.50
C1-C37	1.38	1.48	0.10	1.37	1.47	0.10	1.36
C2-C38	1.51	1.54	0.03	1.52	1.54	0.02	1.52
C1-C4	1.46	1.44	0.02	1.47	1.44	0.03	1.47
C37-C40	1.46	1.44	0.02	1.47	1.44	0.03	1.47
C2-C3	1.36	1.40	0.04	1.36	1.40	0.04	1.35
C38-C39	1.36	1.40	0.04	1.36	1.40	0.04	1.35
C1-C2-C3	134.05	133.19	0.86	132.20	132.27	0.07	132.69
C2-C3-C15	120.19	119.02	1.17	120.03	119.08	0.95	119.40
C2-C3-C26	123.43	122.75	0.68	125.95	125.33	0.62	126.01
C2-C1-C4	136.31	135.59	0.72	135.79	137.49	1.70	135.03
C1-C4-C5	121.54	121.25	0.29	121.36	122.65	1.29	121.22
C1-C2-C3-C15	-21.39	-24.64	3.25	-12.30	-15.16	2.86	-12.14
C37-C38-C39-C51	-21.39	-24.64	3.25	-12.31	-15.16	2.85	-12.14
(**3**)C2-C3-C26-C35	-41.26	-29.59	11.67	-40.37	-31.90	8.47	-39.45
(**4**)C38-C39-C62-C71	-41.26	-29.58	11.68	-40.37	-31.90	8.47	-39.44
(**2**)C2-C3-C15-C16	-48.36	-41.51	6.85	-53.59	-49.96	3.63	-51.96
(**5**)C38-C39-C51-C52	-48.36	-41.51	6.85	-53.59	-49.97	3.62	-51.96
(1)C2-C1-C4-C5	**-46.06**	**-31.42**	**14.64**	**-45.70**	**-38.94**	**6.76**	**-46.60**
(6)C38-C37-C40-C41	**-46.06**	**-31.43**	**14.63**	**-45.69**	**-38.93**	**6.76**	**-46.60**

[a]Ref. 28

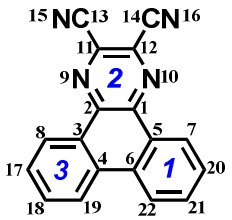

DCPP

Table S8 Selected bond lengths (in Å), bond angles (in deg) and dihedral angles (in deg) of solution-phase and solid-phase **DCPP** at the $\mathbf{S_0}$ ($\mathbf{S_1}$) optimized geometry.

	solution phase			solid phase			
	$\mathbf{S_0}$	$\mathbf{S_1}$	$\lvert\Delta(\mathbf{S_0}\text{-}\mathbf{S_1})\rvert$	$\mathbf{S_0}$	$\mathbf{S_1}$	$\lvert\Delta(\mathbf{S_0}\text{-}\mathbf{S_1})\rvert$	Crystal[a]
C1-C2	1.42	1.39	0.03	1.42	1.38	0.04	1.40
C2-C3	1.45	1.45	-0.00	1.45	1.46	-0.01	1.46
C2-N9	1.34	1.37	-0.03	1.34	1.37	-0.03	1.35
N9-C11	1.32	1.35	-0.03	1.32	1.35	-0.03	1.33
C11-C13	1.44	1.43	0.01	1.44	1.43	0.01	1.45
C1-C2-C3	120.36	119.62	0.74	120.29	119.55	0.74	120.31
(3)C1-C2-C3-C4	**-0.09**	**-0.06**	**-0.03**	**0.73**	**1.26**	**-0.53**	**1.20**
(1)C2-C1-C5-C6	**-0.12**	**-0.07**	**-0.05**	**-0.96**	**-1.31**	**0.35**	**-1.53**
N10-C1-C2-C3	-179.81	-179.83	0.02	179.23	179.20	0.03	179.64
N9-C2-C1-C5	-179.79	-179.83	0.04	-179.25	-179.41	0.16	-178.75
C11-N9-C2-C3	179.88	179.88	0.00	-177.92	-176.63	-1.29	-178.97
C12-N10-C1-C5	179.86	179.87	-0.01	178.28	177.06	1.22	178.45
C3-C2-C1-C5	0.25	0.25	0.00	-0.40	-0.43	0.03	0.04

[a]Ref. 57

Table S9 Selected normal modes j of $\mathbf{S_0}$ with large relaxation energies ($\lambda_j \geqq 1$ meV), as well as frequencies of each mode ω_j, Huang-Rhys factors (S_j) for **HPDMCb** in both solution and solid phases.

solution			solid		
ω_j (cm^{-1})	S_j	λ_j (meV)	ω_j (cm^{-1})	S_j	λ_j (meV)
24	31.429	94.21	48	1.576	9.40
51	3.312	20.86	50	0.706	4.37
56	1.171	8.10	70	2.999	25.86
59	1.037	7.63	78	1.004	9.75
71	0.359	3.14	82	0.241	2.45
78	2.106	20.40	98	0.272	3.29
89	0.330	3.63	104	0.153	1.97
119	0.072	1.07	111	0.133	1.84
151	0.115	2.16	117	0.542	7.89
186	0.701	16.12	123	0.092	1.40
258	0.377	12.03	127	0.532	8.36
263	0.238	7.75	141	0.276	4.81
309	0.043	1.63	141	0.780	13.66
423	0.045	2.34	158	1.541	30.12
502	0.017	1.04	177	0.064	1.41
546	0.128	8.66	205	0.996	25.31
557	0.066	4.56	271	0.320	10.76
716	0.026	2.33	278	0.086	2.95
781	0.024	2.30	434	0.069	3.71
792	0.018	1.76	437	0.029	1.57
864	0.016	1.70	439	0.039	2.11
912	0.061	6.94	451	0.019	1.06
940	0.014	1.60	515	0.020	1.27
1020	0.022	2.79	571	0.026	1.81
1063	0.025	3.31	573	0.171	12.17
1067	0.010	1.37	627	0.034	2.68
1097	0.408	55.55	736	0.012	1.11
1119	0.013	1.73	740	0.021	1.91
1120	0.017	2.34	772	0.015	1.40
1208	0.056	8.39	793	0.019	1.89
1210	0.043	6.47	796	0.025	2.52
1212	0.020	3.01	804	0.015	1.48
1215	0.126	18.91	912	0.077	8.72
1265	0.052	8.13	1070	0.017	2.30
1326	0.009	1.40	1081	0.016	2.21
1356	0.026	4.30	1101	0.357	48.71
1492	0.025	4.67	1218	0.149	22.52

1536	0.048	9.07	1221	0.011	1.72
1624	0.818	164.83	1223	0.015	2.32
1657	0.100	20.56	1272	0.060	9.46
1679	0.081	16.81	1330	0.027	4.40
1682	0.015	3.07	1363	0.021	3.50
1752	0.005	1.15	1499	0.012	2.22
			1541	0.029	5.50
			1555	0.007	1.26
			1634	0.672	136.12
			1662	0.083	17.01
			1667	0.029	6.01
			1685	0.069	14.47
			1687	0.007	1.43
			1755	0.032	6.86

Table S10 Selected normal modes j of $\mathbf{S_0}$ with large relaxation energies ($\lambda_j \geqq 1$ meV), as well as frequencies of each mode ω_j, Huang-Rhys factors (S_j) for **DCPP** in both solution and solid phases.

solution			**solid**		
ω_j (cm^{-1})	S_j	λ_j (meV)	ω_j (cm^{-1})	S_j	λ_j (meV)
111	0.172	2.38	128	0.119	1.89
235	0.208	6.08	250	0.152	4.71
357	0.115	5.09	351	0.029	1.26
414	0.978	50.16	369	0.066	3.00
495	0.342	21.01	419	1.022	53.14
615	0.205	15.60	468	0.017	1.00
715	0.184	16.34	511	0.370	23.46
817	0.029	2.91	619	0.253	19.46
1080	0.050	6.77	721	0.017	1.53
1155	0.029	4.10	723	0.162	14.50
1272	0.008	1.24	825	0.036	3.72
1312	0.079	12.77	1087	0.071	9. 60
1346	0.008	1.31	1112	0.014	1.88
1376	0.026	4.41	1164	0.035	5.01
1408	0.041	7.10	1331	0.099	16.32
1431	0.008	1.46	1390	0.013	2.25
1525	0.019	3.67	1423	0.026	4.64
1589	0.238	46.97	1536	0.034	6.57
1640	0.128	25.98	1596	0.232	45.86
1684	0.195	40.73	1646	0.125	25.43
2386	0.005	1.48	1695	0.209	44.00

Table S11 Selected normal modes j with large relaxation energies (λ_j), as well as frequencies of each mode ω_j, dimensionless displacement (Δ_j) and Huang-Rhys factors (S_j) for ground-state **HPDMCb** in both solution and solid phases. The corresponding vibration type is underlined.

mode j	ω_j (cm^{-1})	Δ_j	S_j	λ_j (meV)	Vibration types[a]
			solution		
3	24	7.928	31.429	94.21	i (1,6,2,5-rings twisting), ii (1,6-rings)
6	51	2.574	3.312	20.86	i (2,5,3,4-rings twisting), ii (1,6-rings)
20	186	1.184	0.701	16.12	i (1,6,3,4-rings and cyclobutene deformation)
116	1097	0.904	0.408	55.55	iv (all benzene rings), v (all benzene rings and cyclobutene, iii (cyclobutene)
136	1215	0.501	0.126	18.91	iv (all benzene rings), v (all benzene rings and cyclobutene)
166	1624	1.279	0.818	164.83	iv (1,6,3,4-rings), v (3,4-rings and cyclobutene), iii (cyclobutene)
			solid		
4	70	-2.449	2.999	25.86	i (2,5,3,4-rings twisting)
16	141	1.249	0.780	13.66	i (all benzene rings twisting)
20	205	-1.411	0.996	25.31	i (1,6,3,4-rings and cyclobutene deformation)
116	1101	-0.845	0.357	48.71	iv (all benzene rings), v (all benzene rings and cyclobutene), iii (cyclobutene)
129	1218	0.546	0.149	22.52	iv (all benzene rings), v (all benzene rings and cyclobutene)
166	1634	1.159	0.672	136.12	iv (1,6,3,4-rings), v (3,4-rings and cyclobutene), iii (cyclobutene)

[a]**Vibration types**: (**i**) benzene (heterocyclic) ring out-of-plane deformation/twisting vibration; (**ii**) CH out-of-plane rocking vibration; (**iii**) CCC in-plane bending vibration; (**iv**) CH in-plane bending vibration; (**v**) CC stretching vibration.

Table S12 Selected normal modes j with large relaxation energies (λ_j), as well as frequencies of each mode ω_j, dimensionless displacement (Δ_j) and Huang-Rhys factors (S_j) for ground-state **DCPP** in both solution and solid phases. The corresponding vibration type is underlined.

mode j	ω_j (cm^{-1})	Δ_j	S_j	λ_j (meV)	Vibration types[a]
			solution		
5	111	-0.587	0.172	2.38	iii (C11C13N15, C12C14N16), iv (C13N15, C14N16)
9	235	-0.646	0.208	6.08	iv (1,3-rings CH)
16	414	-1.399	0.978	50.16	iii (1,3-rings CCC, C2C3C4, C1C5C6)
57	1312	0.396	0.079	12.77	iv (1,3-rings CH), v (all-rings CC, 2-ring CN)
69	1589	-0.691	0.238	46.97	iii (1,3-rings CCC, 2-ring CNC), iv (1,3-rings CH), v (all-rings CC)
73	1684	0.625	0.195	40.73	iii (1,3-rings CCC), iv (1,3-rings CH), v (1,3-rings CC)
			solid		
2	128	-0.487	0.119	1.89	iii (C11C13N15, C12C14N16), iv (C13N15, C14N16)
9	250	-0.551	0.152	4.71	iv (1,3-rings CH)
15	419	1.430	1.022	53.14	iii (1,3-rings CCC, C2C3C4, C1C5C6)
57	1331	0.445	0.099	16.32	iv (1,3-rings CH), v (all-rings CC, 2-ring CN)
69	1596	-0.681	0.232	45.86	iii (1,3-rings CCC, 2-ring CNC), iv (1,3-rings CH), v (all-rings CC)
73	1695	-0.647	0.209	44.00	iii (1,3-rings CCC), iv (1,3-rings CH), v (1,3-rings CC)

[a]**Vibration types**: (**i**) benzene (heterocyclic) ring out-of-plane deformation/twisting vibration; (**ii**) CH out-of-plane rocking vibration; (**iii**) CCC (CNC, CCN) in-plane bending vibration; (**iv**) CH (CN) in-plane bending vibration; (**v**) CC (CN) stretching vibration.

Table S13 The predicted harmonic vibrational frequencies at the minimum of $\mathbf{S_0}$ for **HPDMCb** in acetonitrile solution at the PBE0/6-31G* level.

Harmonic vibrational frequencies / cm^{-1}									
17	22	24	33	45	51	54	56	59	67
71	78	78	89	91	103	119	128	151	186
209	216	227	245	252	252	258	263	290	307
309	415	415	416	418	418	423	423	431	463
463	481	502	542	546	556	557	599	622	625
626	630	630	631	631	659	665	670	687	710
713	714	714	716	716	729	741	752	754	781
781	792	793	802	802	863	864	865	865	866
866	912	922	935	937	940	940	943	952	971
983	984	984	985	985	985	1006	1008	1009	1010
1010	1010	1012	1018	1019	1019	1019	1020	1020	1063
1063	1067	1067	1069	1071	1097	1110	1117	1117	1119
1119	1120	1137	1187	1187	1187	1187	1188	1188	1208
1209	1210	1211	1211	1212	1215	1239	1265	1324	1326
1346	1347	1349	1352	1354	1356	1378	1380	1380	1381
1382	1383	1403	1492	1494	1494	1495	1497	1497	1536
1544	1544	1547	1548	1554	1624	1647	1652	1652	1653
1654	1657	1667	1677	1677	1679	1681	1682	1686	1752
3211	3211	3212	3212	3214	3215	3217	3217	3218	3218
3222	3222	3225	3225	3227	3227	3231	3231	3231	3231
3233	3233	3239	3239	3240	3240	3240	3240	3244	3244

Table S14 The predicted harmonic vibrational frequencies at the minimum of $\mathbf{S_1}$ for **HPDMCb** in acetonitrile solution at the PBE0/6-31G* level.

Harmonic vibrational frequencies / cm^{-1}									
7	21	33	33	49	51	59	62	73	73
80	87	93	96	105	109	122	134	152	156
196	222	228	240	249	261	264	269	284	310
313	397	397	412	412	416	421	424	430	450
461	476	489	515	527	541	544	597	611	620
624	627	627	627	629	633	651	666	684	701
701	704	711	711	712	729	732	736	749	773
775	784	786	792	795	848	853	854	859	862
862	886	903	926	932	932	934	937	941	962
982	983	983	985	986	986	986	1003	1004	1004
1005	1006	1006	1009	1010	1011	1012	1014	1015	1059
1060	1062	1064	1066	1066	1103	1111	1119	1119	1122
1123	1132	1146	1167	1186	1186	1186	1186	1187	1187
1202	1208	1208	1211	1212	1214	1244	1263	1328	1329
1340	1343	1345	1355	1363	1364	1381	1383	1386	1386
1388	1392	1399	1442	1463	1492	1492	1494	1498	1500
1502	1533	1534	1537	1538	1545	1546	1597	1627	1628
1629	1629	1639	1640	1659	1660	1660	1666	1672	1677
3212	3212	3213	3213	3214	3214	3218	3218	3220	3220
3221	3221	3228	3228	3231	3231	3233	3233	3235	3236
3237	3237	3240	3241	3242	3243	3243	3246	3249	3250

Table S15 The predicted harmonic vibrational frequencies at the minimum of $\mathbf{S_0}$ for **HPDMCb** in crystal at the PBE0/6-31G* level.

Harmonic vibrational frequencies / cm^{-1}									
48	50	67	70	78	82	85	98	104	111
117	123	127	133	141	141	154	158	177	205
220	230	232	253	263	271	273	278	296	317
322	425	432	434	437	439	442	445	451	477
483	495	515	555	557	571	573	607	627	629
630	634	635	636	637	671	672	679	689	718
727	732	736	738	740	743	747	755	772	793
796	804	806	812	816	878	879	883	886	888
892	912	929	946	949	952	953	959	962	975
986	989	995	998	998	1002	1006	1010	1011	1014
1014	1017	1019	1022	1023	1024	1025	1026	1027	1069
1070	1072	1075	1079	1081	1101	1117	1121	1123	1125
1133	1137	1145	1196	1196	1202	1206	1215	1218	1219
1220	1221	1223	1225	1229	1229	1244	1272	1326	1330
1353	1355	1356	1359	1362	1363	1393	1395	1396	1397
1402	1407	1409	1499	1501	1501	1502	1508	1508	1541
1546	1547	1554	1555	1558	1634	1656	1658	1658	1662
1664	1667	1676	1685	1686	1687	1689	1691	1691	1755
3214	3215	3215	3216	3218	3218	3223	3224	3224	3230
3232	3233	3237	3241	3243	3244	3244	3245	3245	3246
3248	3249	3250	3254	3255	3258	3262	3262	3277	3278

Table S16 The predicted harmonic vibrational frequencies at the minimum of $\mathbf{S_1}$ for **HPDMCb** in crystal at the PBE0/6-31G* level.

Harmonic vibrational frequencies / cm^{-1}									
41	44	65	76	81	83	94	98	102	113
117	120	126	128	134	145	156	161	169	190
208	234	234	249	265	266	274	277	297	320
321	413	418	425	429	432	436	440	442	464
475	489	498	523	543	552	555	604	616	625
627	629	631	632	632	640	658	665	685	711
715	720	725	732	732	734	740	745	757	782
789	795	799	800	803	860	870	873	874	885
885	891	903	932	936	944	946	951	956	968
984	987	989	996	996	997	997	1008	1009	1009
1011	1013	1014	1015	1016	1018	1018	1021	1022	1066
1069	1070	1072	1072	1073	1117	1118	1123	1124	1132
1133	1141	1151	1180	1193	1194	1204	1205	1206	1210
1217	1217	1219	1225	1226	1228	1250	1267	1329	1332
1347	1349	1351	1358	1368	1368	1392	1394	1395	1397
1407	1417	1421	1452	1493	1497	1498	1500	1504	1506
1532	1536	1541	1543	1544	1553	1553	1609	1631	1631
1636	1636	1649	1650	1668	1669	1671	1673	1679	1684
3213	3214	3214	3215	3218	3219	3224	3225	3226	3226
3234	3234	3238	3239	3240	3246	3249	3249	3251	3251
3252	3252	3253	3254	3258	3259	3265	3268	3283	3283

Table S17 The predicted harmonic vibrational frequencies at the minimum of $\mathbf{S_0}$ for **DCPP** in THF solution at the PBE0/6-31G* level.

Harmonic vibrational frequencies / cm^{-1}									
17	66	75	95	111	111	171	180	235	253
272	317	357	369	406	414	431	456	489	495
496	557	564	567	597	615	627	686	706	714
715	735	744	764	787	800	817	834	890	898
960	975	987	1017	1019	1026	1080	1084	1102	1155
1164	1179	1199	1200	1269	1272	1312	1338	1346	1376
1398	1408	1431	1481	1500	1507	1525	1557	1589	1601
1640	1658	1684	1691	2386	2389	3227	3229	3240	3243
3250	3258	3258	3265						

Table S18 The predicted harmonic vibrational frequencies at the minimum of $\mathbf{S_1}$ for **DCPP** in THF solution at the PBE0/6-31G* level.

Harmonic vibrational frequencies / cm^{-1}									
31	63	77	81	111	118	153	162	236	253
259	281	351	371	383	403	416	417	473	491
493	503	533	548	575	598	598	660	664	691
698	704	709	730	747	767	797	816	888	900
947	971	986	991	1010	1020	1021	1061	1066	1077
1154	1157	1167	1183	1186	1226	1274	1324	1325	1345
1390	1396	1426	1443	1459	1476	1477	1523	1530	1558
1567	1606	1638	1695	2335	2358	3244	3245	3255	3260
3267	3271	3271	3285						

Table S19 The predicted harmonic vibrational frequencies at the minimum of $\mathbf{S_0}$ for **DCPP** in crystal at the PBE0/6-31G* level.

Harmonic vibrational frequencies / cm^{-1}									
100	128	133	145	173	177	220	231	250	270
320	351	369	376	419	449	468	490	504	511
534	575	588	597	619	622	634	692	721	723
737	743	774	798	825	847	860	863	942	958
967	1010	1031	1036	1053	1080	1087	1100	1112	1164
1173	1189	1220	1221	1257	1296	1331	1352	1361	1390
1417	1423	1443	1493	1510	1514	1536	1566	1596	1612
1646	1667	1695	1699	2391	2400	3236	3248	3254	3263
3268	3275	3295	3297						

Table S20 The predicted harmonic vibrational frequencies at the minimum of $\mathbf{S_1}$ for **DCPP** in crystal at the PBE0/6-31G* level.

Harmonic vibrational frequencies / cm^{-1}									
102	118	132	144	146	154	197	201	246	263
296	310	362	376	407	423	429	439	499	503
512	515	559	561	593	601	609	669	686	699
706	731	734	737	767	797	814	822	914	923
952	983	999	1005	1037	1038	1061	1069	1071	1082
1163	1165	1175	1193	1195	1242	1296	1324	1334	1356
1398	1407	1433	1461	1468	1482	1486	1532	1554	1572
1574	1617	1645	1706	2344	2370	3245	3257	3259	3266
3277	3282	3301	3304						

Reference

(S1) Wolf, E. *Progress in Optics*; North-Holland Publishing Company: AmsterDam-London, 1972.

(S2) Turro, N. J.; Ramamurthy, V.; Scaiano, J. C. *Modern Molecular Photochemistry of Organic Molecules*; University Science Books: Sausalito, CA, 2010.

(S3) Send, R.; Furche, F. First-Order Nonadiabatic Couplings from Time-Dependent Hybrid Density Functional Response Theory: Consistent Formalism, Implementation, and Performance. *J. Chem. Phys.* **2010**, *132*, 044107.

(S4) Yan, Y. J.; Mukamel, S. Eigenstate-Free, Green Function, Calculation of Molecular Absorption and Fluorescence Line Shapes. *J. Chem. Phys.* **1986**, *85*, 5908-5923.